Temperature-induced evolution of subsurface nanocavities in argon-implanted copper

O. Kurnosikov,[1,*] D. V. Kulikov,[2,3] V. S. Kharlamov,[2,3] H. J. M. Swagten,[1] and Yu. V. Trushin[2,3]

[1]*Department of Applied Physics, cNM, Eindhoven University of Technology, 5600 MB Eindhoven, The Netherlands*

[2]*Saint Petersburg Academic University-Nanotechnology Research and Education Center RAS, St. Petersburg, 194021, Russia*

[3]*A. F. Ioffe Physical-Technical Institute of RAS, St. Petersburg, 195220, Russia*

(Received 11 January 2011; revised manuscript received 2 May 2011; published 12 August 2011)

The evolution of argon-filled nanocavities in a copper crystal under annealing is studied experimentally and theoretically. The subsurface argon-filled nanocavities are formed after a short annealing at a temperature ∼1000 K by coalescence of subsurface defects initially created by argon implantation. The further prolonged annealing at a temperature above 1075 K leads to decomposition of the nanocavities and diffusion of implanted argon out of the sample. According to a simple analysis, the mechanism of the nanocavity formation is governed not only by the migration of simplest defects, such as vacancies and argon and copper interstitials, but also to a large extent, by diffusion and interaction of the complexes of these simplest defects. The experimental studies with x-ray photoelectron spectroscopy and scanning tunneling microscopy and spectroscopy provide valuable data sets of the density of nanocavities and their size and depth distribution. Based on the experimental results, a theoretical model is developed. The calculation with the model proves that the growth of the nanocavities is mainly determined by the temperature-induced migration of vacancy-argon complexes. By combining the experimental data with the simulation results, the migration energy of these kinds of complexes is estimated ∼2.55–2.75 eV. Moreover, the calculation with our model provides the estimate of the dissociation energy of a multiple complex, consisting of two vacancies and two argon atoms, as 1.10–1.18 eV. These parameters, reported in this article, play a key role in the description of the kinetics of the growth and decomposition of nanocavities.

DOI: 10.1103/PhysRevB.84.054109 PACS number(s): 61.72.Cc, 61.72.J−, 61.72.U−, 68.37.Ef

I. INTRODUCTION

Study of metals irradiated with ions of noble gases is stimulated by modern technology, in which ion beams or plasma with the ion energy of the order of 1 keV are used for etching, sputtering, and deposition of micro- and nanostructures.[1,2] In addition to the main sputtering-deposition processes, different kinds of defects of a crystalline lattice, such as vacancies, interstitials, and their complexes, are induced near a surface under the ion irradiation. Further evolution of the defects can lead to their aggregation in clusters, forming nanocavities filled with the implanted gas. All these defects affect the structural and electronic properties of materials and reduce the reliability and lifetime of electronic devices. Therefore, a study of the evolution of the irradiation-induced defects leading to the subsurface nanocavities is required for technological applications.

Besides the application issue, the subsurface nanocavities may be exploited in the studies of basic aspects of nanophysics. Recently, it has been shown that the subsurface nanocavities in metals induce near-surface quantum wells (QW)[3–8] as well as several other interesting effects such as electron interference at the surface[6] and diffraction of internal electrons from a nanostructured interface.[7] Because the observation of all these effects is strongly dependent on the size, shape, and depth of the nanocavities and their interface structure, a study of the formation and evolution of subsurface nanocavities is of great scientific importance.

Although the defects in metals induced by ion irradiation have been studied for decades,[9,10] many aspects of defect evolution are still not clear. Particularly, the scenario of the formation of subsurface nanocavities under irradiation with heavy ions of noble gases, such as argon, widely used in the technology, has not been studied in detail. The lack of scrutinized reports on this subject can be explained by the difficulties of experimental observation and analysis of the separate defects hidden under a surface of metals. In many cases, convenient experimental techniques reveal integral characteristics of the defects across the sample or provide data with resolution much lower than the size of a nanocavity or even the average distances between them.

If one considers only a free migration of the simplest defects, such as vacancies and interstitial argon atoms, the formation of nanocavities should already start during the irradiation at room temperature due to quite low migration energies of both the vacancy and interstitial argon atom. However, our experimental results show that this process begins at a significantly higher temperature and requires postannealing. This means that at room temperature, all interstitial Ar atoms and vacancies together form some other defect states with higher migration energies, thereby slowing down the processes of the nanocavity formation. A more realistic approach should additionally include the migration of vacancy-argon complexes as well as the evolution of multiple complexes of these kinds of defects.

The actual scenario of nanocavity formation is determined by a variety of kinetic parameters (e.g., migration and dissociation energies) of these complex defects. There is no reliable data in the literature concerning both the physical nature of these complexes and their energy values. Particularly, these values determine the concentration of nanocavities and their size distribution under different annealing temperatures. If this concentration and distribution can be determined in a specific experiment, it could be possible to solve the inverse problem and find the set of the migration and binding energies of these defect states by using the experimental data. This approach requires an adequate physical model taking into

account the nature and structure of the considered defect complexes.

In this paper, we present a kinetic model of the growth of nanocavities as a result of the diffusion of defects in copper induced by Ar irradiation. The model operates with an experimental data set, including the concentration of nanocavities and their depth and size distribution attributed to annealing temperatures. Because the standard methods of subsurface analysis cannot provide a whole set of the required data or they are not robust enough, we exploited a surface-sensitive scanning tunnel microscopy and spectroscopy (STM and STS) technique for subsurface characterization. A detailed description of how this inconvenient application of the STM and STS technique was successfully utilized to obtain data on the subsurface nano-objects is presented in the first part of our report. We also used a standard x-ray photoelectron spectroscopy (XPS) method supporting our data obtained by the STM and STS measurements. Finally, by computer simulation and approximation of the experimental data, the migration and binding energies for the complexes of vacancies and argon atoms are determined.

II. EXPERIMENT

We carried out the experimental studies of the formation and evolution of subsurface nanocavities in a copper sample and defined the density of the nanocavities as well as the distribution of their depth and size at different annealing temperatures. As mentioned above, these data are obtained with two experimental techniques: the STM and STS and XPS.

A single crystal of copper was used for the implantation of the Ar ions, forming various subsurface defects in the Cu crystalline lattice. The Cu samples with two different low-index surface orientations, Cu(001) and Cu(110), were used in the experiment. The third low-index surface orientation of the sample, Cu(111), is not suitable for the STS analysis of subsurface nanocavities. The electronic band structure of Cu in the ⟨111⟩ direction reveals no bulk electronic states that are used for the subsurface STM and STS detection.

The preparation of samples and all subsequent characterizations were done in-situ in the ultrahigh vacuum (UHV) setup with the base pressure of 10^{-10} mbar. After a standard procedure of cleaning, the copper samples were irradiated for $t_{irr} = 1800$ s with the Ar ion flux of $F_{Ar} = 1.4 \times 10^{14}$ cm^{-2}s^{-1} with the ion energy of $E_{Ar} = 5$ keV at the temperature of the substrate of $T_{irr} = 300$ K. As well known, the Ar bombardment leads to the sputtering of the upper layers of Cu sample away inducing some additional surface roughness. However, we actually use another effect of Ar irradiation. The Ar irradiation also results in the subsurface ion implantation on the typical depth of about 10 nm as well as in the formation of the subsurface defects of the crystalline lattice on the same depth scale. Actually, only a part of irradiation dose of Ar is absorbed by the sample near its surface. We will come to this issue later.

After the ion irradiation, the sample was annealed at T_{1ann} in the range of 1000–1070 K for $t_{1ann} = 300$ s. This annealing makes the surface smooth and initiates the growth of the subsurface nanocavities. At the final stage of the experiment, an extra annealing, at $T_{2ann} = 1075$–1150 K for $t_{2ann} = 1200$ s, was done to remove all argon implanted in the sample. Before the annealing and after each temperature treatment, the samples were analyzed with the XPS method to monitor the argon content in copper close to the surface. A detailed study of the annealed samples with the STM and STS method was carried out as well.

In our experiment, the standard XPS method is capable of analyzing only a fraction of the subsurface Ar content close to the surface. The mean escape length of secondary electrons in copper is of a few nanometers,[11] which is less than the actual depth of Ar estimated as 10 nm. Nevertheless, the XPS analysis, even of the fraction of the subsurface Ar, supplies us with valuable qualitatively data about the content of Ar in the sample, before and after annealing, indicating its evolution.

The application of the STM and STS method in our experiment for the subsurface characterization is inconvenient. However, in spite of the common believe that the STM technique can be exclusively applied to a surface analysis, in some cases, subsurface objects can be detected with STM (Fig. 1). Of course, this detection can be done only if the subsurface object affects surface properties. A subsurface nano-object can locally induce a surface deformation or, alternatively, change electron density at the surface caused by the electron backscattering from the subsurface nano-objects, inducing the electron interference at the surface (Fig. 2). In principle, both these characteristics, the local deformation and the variation of the electron density, can be used to indicate a location of a subsurface inclusion. However, usually the deformation of the surface is so weak and nonlocal that a subsurface nanocavity is frequently not detectable in the STM measurements. On the other hand, the electron scattering or reflection from the subsurface nanocavity affects the electron density at the surface very locally and can be easily registered with the STS technique.

The following explanation helps to understand how the required data set has been deduced from the STS measurements. Electrons, partially confined in copper between the

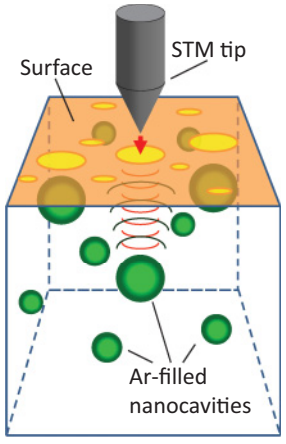

FIG. 1. (Color online) Schema of experiment exploiting the STM and STS technique to determine 2D density of subsurface nanocavities. The subsurface argon-filled nanocavities (green balls) locally affect surface electronic properties above the nanocavities (yellow circles) due to electron backscattering from the buried nano-interface. This variation is detected with an STM probe.

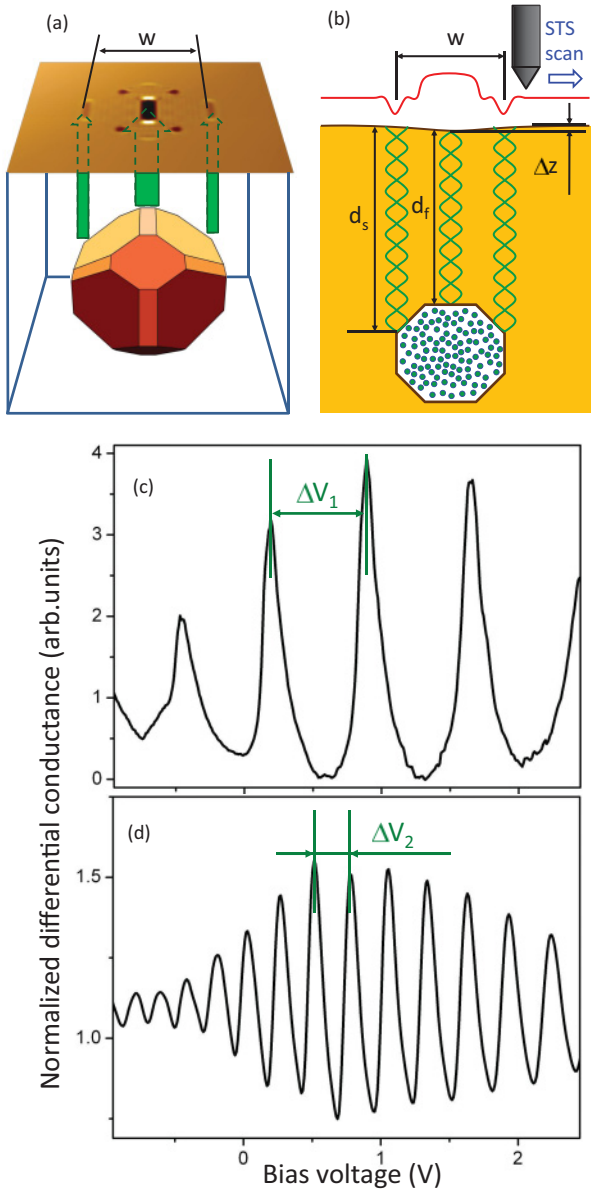

FIG. 2. (Color online) Schema of measurement of size and depth of a nanocavity in the Cu(110) sample. (a) The central spot of the differential conductance map (simulated picture) is induced by electron backscattering from the small (110) facet, whereas other satellite spots are induced by scattering at the edges of the nanocavity. The distance between the satellite spots w characterizes the nanocavity size. Here, the faceted nanocavity is presented by the last atomic layer of copper at the interface, which mainly contributes to the electron scattering. (b) Illustration of the origin of the central and satellite spots in (a) by the side view of the system with Ar-filled faceted nanocavity. The different distances d_f and d_s at the electron reflection and scattering provide various phases of the reflected electron waves coming at the surface. A profile of differential conductance at the STS scanning is schematically shown with the red line. A possible surface deformation Δz caused by the nanocavity, schematically indicated in (b), is negligible. (c) and (d) Experimental plots of normalized differential conductance measured in the center of the main spot corresponding to two different nanocavities. The oscillation periods $\Delta V_1 \approx 0.7\ V$ and $\Delta V_2 \approx 0.3\ V$ are determined by the depths of location of the (110) facets d_f of the different nanocavities, which are equal to 3.5 nm and 8 nm, respectively.

surface and subsurface nanocavity, form the QW resonances [Fig. 2(b)]. The QW resonances lead to variation of differential conductance measured at the surface by the STS technique. These resonances are registered just above each nanocavity within a spot size of between 3 and 10 nm. Usually, the size of the spot is less than the actual size of the faceted nanocavity because the QW resonances are induced by only the upper facet parallel to the surface. Nevertheless, counting the number of spots per surface unit, the two-dimensional (2D) density of nanocavities can be deduced.

The depth of nanocavity location can be found analyzing the electron energy difference ΔE between two neighboring QW resonances in the center of the spot or the period of oscillation ΔV of the differential conductance [Figs. 2(c) and 2(d)]. This period is determined by the depth of location d of the reflecting facet using the formula:

$$d = \frac{\pi}{\Delta E}\frac{dE}{dk}, \tag{1}$$

where k is the wave number of the electron in the direction perpendicular to the surface; E is electron energy: $\Delta E = e\Delta V$. Using a set of the oscillation periods within different spots, the depth distribution of the nanocavities can be deduced.

Regarding the size of nanocavity, it cannot be accurately deduced from the spot size in a general case: only a part of interface at the nanocavity is responsible for the QW formation. However, in the particular case of the Cu(110) sample, there is a possibility to register the actual size of the nanocavity. This possibility is because the nanocavity in the Cu(110) sample induces several satellite spots accompanying the central one (Fig. 2). These satellite spots originate from electron scattering on some facet edges at the sides of the nanocavity. The satellite spots are formed on the Cu(110) surface because the focusing effect[12] enhances the electron propagation in the [110] direction perpendicular to the surface. The focusing effect in metals originates from the specific anisotropy of the electron band structure. This effect may concentrate the electron propagation in a few specific directions where the electron wave shows quite a low decay. For the particular Cu(110) cut, this is exactly the case for the perpendicular propagation. Thus, the distance w between the satellite spots on the surface corresponds to the projected distance between the scattering structures at the sides of the nanocavity [Figs. 2(a) and 2(b)]. These scattering structures relate to the known location at the nanocavity interface and used to determine the size of the nanocavity.

Thus, the STM and STS technique in our experiments supplies us with the quantitative data, such as the density of the nanocavities deduced by counting the number of main spots per surface unit (Fig. 1). Moreover, by analyzing the oscillations of the surface conductance within the main spot and measuring the distance between the satellite spots, the depth and size distribution of the subsurface nanocavities can be determined (Fig. 2). A high spatial resolution provided by the STM and STS technique, which is ~0.5 nm in the presented case, is an important factor to achieve the required accuracy of our experimental data.

All the STM and STS measurements were carried out at 77 K in the same UHV setup. Two operation modes of STS measurements were used: (1) mapping the differential

conductance across the atomically flat copper surface by maintaining the bias voltage fixed and keeping the feedback loop closed and (2) measuring the differential conductance dI/dV in some selected locations within the spots above a nanocavity by varying the bias voltage from −1.0 V to +2.5 V with an open feedback loop. A lock-in technique is used for both modes with the modulation of 50 mV peak-to-peak added to the bias voltage. The STS mapping provides the data related to the density and size of the nanocavities, while the dependence dI/dV measured at the selected point of the surface provides the data related to the nanocavity depth.

Although we used two types of the sample cuts, regarding the data on the size distribution, the Cu(110) sample provides more complete information than the Cu(001) one. This is due to a specific anisotropy of the electronic band structure of copper and the focusing effect as mentioned above. Therefore, for the size distribution data set, we mainly used the experimental data obtained on the Cu(110). Other characteristics, such as the density of the nanocavities and depth distribution, measured on the Cu(001) and the Cu(110) samples are consistent.

III. EXPERIMENTAL RESULTS

A. XPS analysis

The XPS analysis of both the Cu(001) and Cu(110) samples shows that the content of argon in the sample decreases with annealing. Figure 3 presents an XPS spectrum of the Cu(110) sample. The XPS spectrum for the Cu(001) sample is reported previously.[6] The XPS spectra of both samples, measured after the Ar bombardment and before annealing, reveal the highest amplitude of two peaks corresponding to the $2p_{3/2}$-$2p_{1/2}$ XPS binding energy of argon. After the annealing at 1000, 1050,[6] and 1070 K (Fig. 3), the amplitude of the $2p_{3/2}$-$2p_{1/2}$ peaks remarkably decreases. The peaks almost disappear after the prolonged annealing at 1075–1150 K[6] (Fig. 3). The most important conclusion drawn from these results is that almost all of the argon leaves the sample under prolonged annealing at 1075–1150 K.

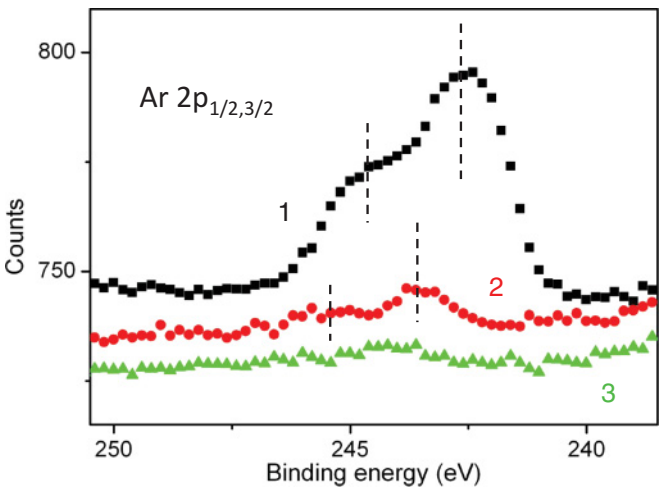

FIG. 3. (Color online) XPS spectra of the Cu(110) sample after Ar implantation without annealing (1) and following annealing at different temperatures: (2) 1070 K for 5 min and (3) 1150 K for 20 min. The position of the peak maxima is schematically marked with the dashed lines.

Besides this conclusion, the XPS spectra show additional qualitative information about the evolution of nanocavites. For the nonannealed sample, the $2p_{3/2}$-$2p_{1/2}$ XPS peaks of binding energy are shifted on several electron volts as compared to the known value of the binding energy for free or adsorbed Ar, which is estimated as $E_{bAr} = 248$ eV[13] (Fig. 3) This shift for Ar implanted in copper originates from a screening by electrons in copper.[14] However, after annealing, the energy shift decreases and the position of the peaks approaches E_{bAr}[6] (Fig. 3). This shows that the influence of the electron screening weakens. It happens only if Ar segregates in clusters filling the nanocavities in copper. Although the shift of the peak positions, associated with nanocavity size, is remarkable, no significant broadening of the full width at half maximum (FWHM) of the peaks in the XPS spectrum is found (Fig. 3). The FWHM may additionally characterize the size variation in an ensemble of nanocavities. This leads to the second important conclusion for the modeling: during annealing, almost all the residual Ar segregates in the clusters of a comparable size. The presence of single Ar atoms or very small agglomerations of Ar atoms in copper should be negligible after annealing. However, the XPS analysis does not provide any reliable quantitative results concerning the concentration and size distribution of nanocavities except some indirect estimations.[15] To obtain these characteristics by direct measurements, the STM and STS technique is used.

B. STM/STS analysis

Prior to STS measurements, we performed STM scans in the constant current mode. The STM images of the samples, annealed after the Ar implantation, reveal many locations on the atomically flat surface where a deformation typically of about 20 pm deep is observed. Figure 4(a) shows an example of the deformation. This deformation, induced by a subsurface nanocavity, spreads over more than 10 nm away from the nanocavity location. However, mainly shallow and large nanocavities induce the detectable deformation, while deep and small ones do not. Therefore, the characterization of the subsurface nanocavities via detection of the surface deformation is not efficient. Nevertheless, the STM images of the surface, obtained with the constant current mode, are useful in our experiments to select the atomically flat terraces prior to the STS measurements.

In contrast to the direct STM detection of surface deformation, the STS mapping, monitoring the perturbation of electronic states by the subsurface nanocavities, provides valuable information. Figures 4(b) and 4(c) present an example of the STS mapping of the same area as in Fig. 4(a). The STS scan above the buried nanocavity reveals a remarkable local variation of the surface differential conductance dependent on the applied bias voltage [Fig. 4(d)]. The signal-to-noise ratio provides a reliable detection of the subsurface nanocavities of different sizes even from deep locations.

If the Cu(110) and Cu(001) samples, prepared at 300 K, were not annealed or were annealed well below 1000 K, up to 450 K, the STS mapping detected no subsurface nanocavities. The slight annealing up to 450 K in some cases is used to

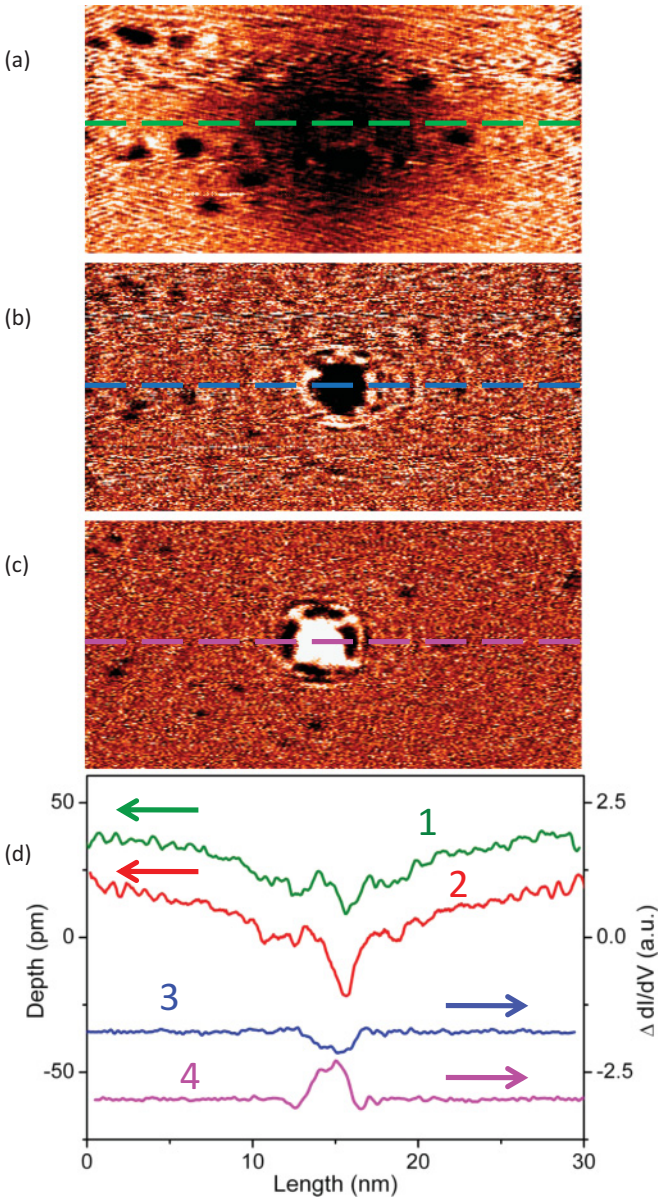

FIG. 4. (Color online) (a) STM and (b) and (c) STS maps (30×15 nm^2) above the same subsurface nanocavity in the Cu(001) sample. The STS maps are scanned with different bias voltage: (b) 0.3 V and (c) 1.0 V and reveal a strong dependence on bias voltage. The STM image in (a) obtained at 0.3 V does not differ remarkably from the image obtained at 1.0 V (not shown). (d) Cross-sections along the dashed lines in (a)–(c). Curves 1 and 2 are the relief measured at 0.3 V and 1.0 V, respectively, and curves 3 and 4 are the profile of differential conductance measured at 0.3 V and 1.0 V, respectively. Curves 3 and 4 are shifted for better visibility.

obtain an atomically flat surface required for an unambiguous treatment of the STS data. At the same time, the STM images of the same sample obtained in the constant current mode shows many screw dislocations at the surface. This is evidence of the radiation damage of the crystalline lattice due to the Ar implantation. Combining this observation with the XPS data, we can conclude that the implanted argon does not segregate in big clusters filling the subsurface nanocavities if the sample was not annealed or was slightly annealed well below 1000 K.

The STS mapping of the samples annealed at 1000 K and slightly higher temperatures reveals the appearance of the spots of variable surface differential conductance induced by subsurface nanocavities. The STM scans reveal significantly fewer structural surface defects in comparison with nonannealed samples. These observations confirm that the segregation of Ar is remarkable in this temperature range. At the same time we do not specify that this temperature is the threshold temperature when the nucleation and initial growth of the nanocavities just starts. This threshold temperature should be lower than 1000 K. However, the smallness of the nanocavities formed at this regime cannot provide reliable experimental data on their size and depth distribution.

After the long annealing at 1075–1150 K, the STS analysis detects no more nanocavities. The STM images reveal a few or no Ar-induced dislocations. This is consistent with the XPS data detecting no Ar in the sample. Therefore, the detailed characterization of the nanocavity distribution was carried out with the samples annealed at 1000–1070 K.

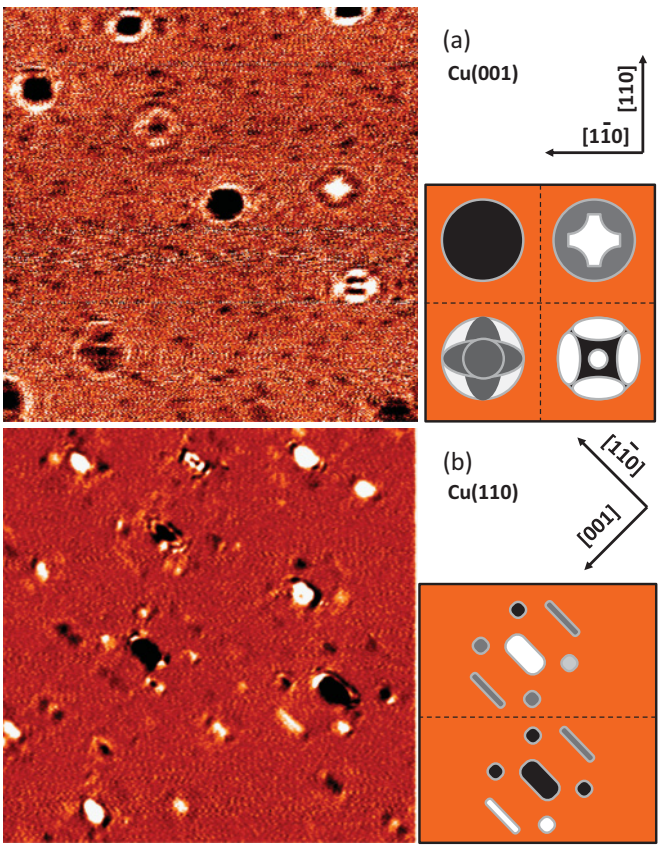

FIG. 5. (Color online) Left panels: differential conductance maps (60×60 nm^2) of (a) Cu(001) and (b) Cu(110) of the samples containing the subsurface nanocavities after annealing. The spots are induced by the subsurface nanocavities. The surface density of nanocavities can be deduced from a set of this type of the STS maps. Right panels: schematic drawing of various structure of the spots (a) for the Cu(001) and (b) for Cu(110) surfaces. Each nanocavity in the Cu(001) sample forms only one spot but with a complex inner structure. Each nanocavity in the Cu(110) sample forms a main spot together with several satellite spots. The contrast within the spots depends on bias voltage and the depth and asymmetry of the nanocavity.

Figures 5(a) and 5(b) present two examples of the spatial distribution of the differential conductivity across the large surfaces of the annealed Cu(001) and Cu (110) samples. The STS mapping of the surface shows many spots of the size varying from 3 to 10 nm, where a variation of differential conductivity is observed. Using a set of this type of images, the mean number of nanocavities per surface unit can be determined. The value of this density is 3.1×10^{11} cm^{-2} and 4.1×10^{11} cm^{-2} for the Cu(001) and Cu(110) samples, respectively. The difference in these numbers for different samples is insignificant for the model calculation.

The dark or light color within the spots observed in the STS images corresponds to a negative or positive deviation of differential conductance from the mean value across the surface, respectively. This deviation quasiperiodically depends on the depth of nanocavity. Therefore, the spots induced by different nanocavities located on slightly different depths appear with different color on the STS maps. The typical spot shape is presented by the schematic drowning in Fig. 5 (right panels). However, as discussed above, the variation of differential conductance also depends on the energy of probed electron states, and this dependence is connected with the depth. Therefore, measuring the dependence of differential conductance on electron energy within each spot provides the data for determining the depth of the nanocavity using formula (1). An example of the experimental dependences, measured in the center of two different spots, is illustrated in Figs. 2(c) and 2(d). The plot reveals the oscillating behavior of the differential conductance as discussed in the previous section. A distribution of the nanocavity depths calculated using a set of oscillating curves obtained on an ensemble of spots is presented in Fig. 6. The mean depth of the nanocavity d_{nm} is of about 12 nm. As separately checked, the STS technique is capable of detecting the subsurface nanocavities in copper at the ultimate depth of about 30 nm. Therefore, the mean value of 12 nm reported above is the real value, which is not reduced by the intrinsic limit of depth sensitivity of the STS analysis.

As previously mentioned, the satellite spots observed on the STS maps of the Cu(110) surface originate from the scattering from the sides of interface and can be used to monitor the

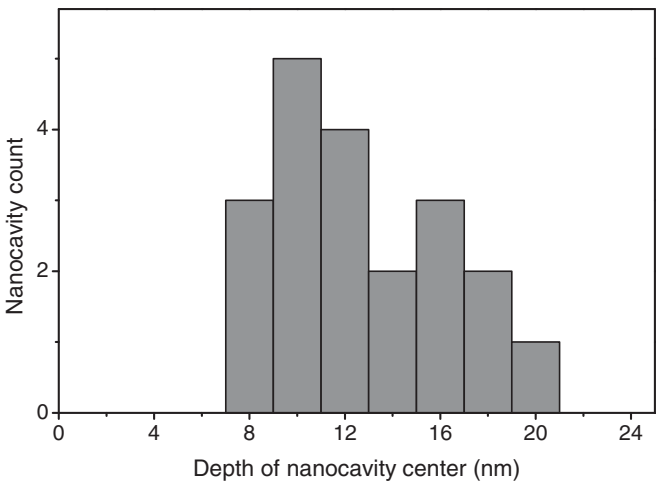

FIG. 6. Histogram of the depth distribution of nanocavities. The depth is counted from the center of nanocavities.

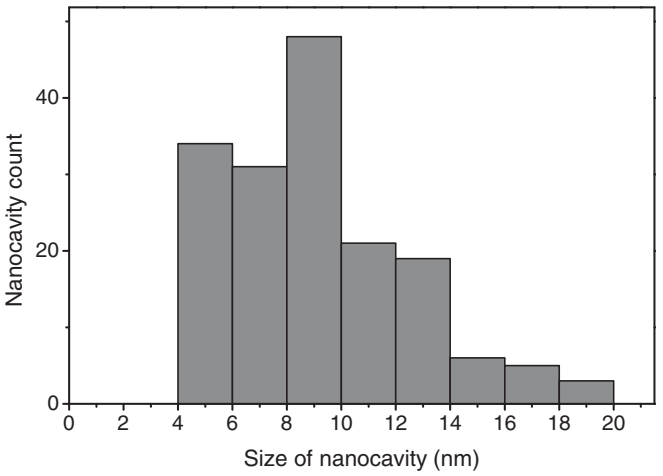

FIG. 7. Histogram of size distribution of the nanocavities. The data for the sizes of up to 4 nm are absent due to low resolution or absence of the satellite spots for the smallest nanocavities.

nanocavity size [Figs. 2(a) and 2(b)]. A histogram of size distribution, obtained by the statistical analysis of the distance between the satellite spots, is presented in Fig. 7. However, this histogram does not represent the data for the smallest sizes of the nanocavities, which are less than 4 nm, because the satellite spots at the smallest nanocavities are not detectable by the STS method. Nevertheless, the absence of the data for the smallest nanocavities does not affect the simulation results significantly, and this fraction of the data can be omitted.

The histogram of size distribution together with the value of nanocavity density can be used to estimate the total amount of Ar captured in the nanocavities N_{capt}. This estimation gives the value of $N_{capt} = 5.9 \times 10^{15}$ cm^{-2}. The total dose of sample irradiation is $N_{irr} = 2.5 \times 10^{17}$ cm^{-2} that is two orders of magnitude higher than N_{capt}. Only 2% of argon is actually captured in the nanocavities regarding the total dose at the irradiation.

There are two reasons for this. First, the losses of argon occur due to sputtering of the copper surface releasing the argon atoms, which were already embedded in the sample during the irradiation. Second, the losses occur due to diffusion of implanted argon away from the near-surface area at both the irradiation and annealing stages. Our model takes into account all these processes of Ar losses.

C. The summary of experimental results

The experimental studies of the formation and evolution of the subsurface nanocavities in the irradiated samples provide a set of data for the model calculation. Based on the XPS and STM and STS analyses, the process of formation and evolution of the nanocavities can be schematically divided in the following three main steps:

(1) Irradiation of copper at room temperature with Ar ions leads to implantation of the Ar atoms in the sample without forming the nanocavities.

(2) Annealing at the temperature of 1000–1070 K for 300 s leads to the formation of the nanocavities and losses of argon. The density of the nanocavities is $\sim 3.1 \times 10^{11}$–4.1×10^{11} cm^{-2}. The nanocavities contain $\sim$2% of argon

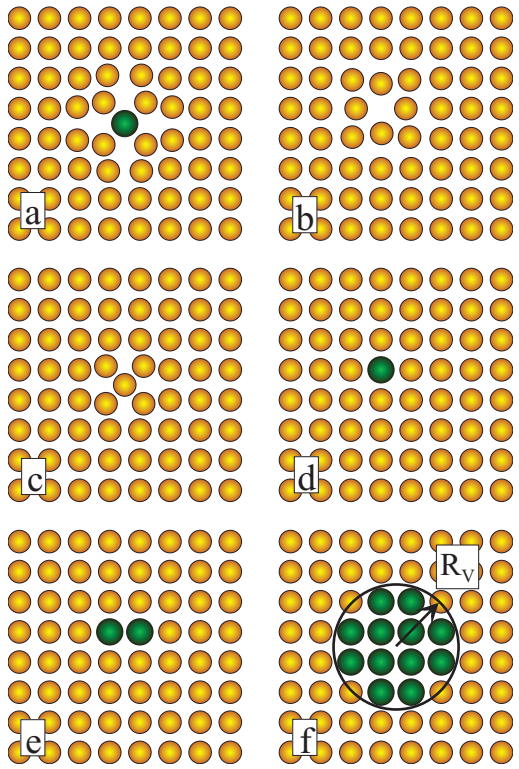

FIG. 8. (Color online) Schematic drawing of the defects considered in the model: (a) The interstitial of argon *Ar*; (b) Vacancy in copper crystalline lattice *v*; (c) The interstitial of copper *i*; (d) The single complex of argon and vacancy *vAr*; (e) The double vacancy-argon complex 2*vAr*; (f) A multiple vacancy-argon complex is considered as a nanocavity with radius RV.

considering the initial irradiation dose. The mean depth of the nanocavities is about 12 nm, and their size distribution is represented by the histogram shown in Fig. 7.

(3) After annealing at the temperature of 1075–1150 K for 1200 s, argon diffuses away from the sample, and the nanocavities disappear.

We used these experimental data together with the characteristics already known for defects in copper for determining the values of the migration and binding energies of Ar complexes in copper as described in the next sections.

IV. MODEL

A. General approach

During Ar-irradiation and subsequent annealing, different kinds of defects in copper substrate are formed as schematically depicted in Fig. 8. For the sake of brevity, we introduce index j associated with each considered type of defects. When argon ion penetrates the crystalline lattice of copper substrate, it forms Ar interstitial defect state $j = Ar$ [Fig. 8(a)]. Excess of kinetic energy of Ar at the entrance of copper crystal additionally induces some disorder of crystalline lattice by forming vacancies $j = v$, and copper interstitials $j = i$ [Figs. 8(b) and 8(c)]. In principle, the appearance of only these three types of defects ($j = v, i,$ or Ar) should be expected at a low irradiation dose if all these defects can be considered as immobile. Actually, this is not the case. The defects can migrate due to thermally activated diffusion. The process of diffusion is described by the corresponding diffusion coefficient D_j, which is governed by the corresponding migration energy $\varepsilon^m{}_j$, in accordance to a common approach:

$$D_j = D_j^0 \exp\left(-\varepsilon_j^m / kT\right). \tag{2}$$

Here k is Boltzmann constant, and T is temperature. Because of the migration energies for interstitials $\varepsilon^m{}_i = 0.12$ eV,[16] vacancies $\varepsilon^m{}_v = 0.7$ eV,[17] and Ar interstitials $\varepsilon^m{}_{Ar} = 0.7$ eV[18], all three types of the simplest defects are mobile already at 300 K, i.e., without sample annealing.

The mobility of defects can lead to a significant change of defect concentration as well as to the formation of other kinds of defects, namely, the defect complexes. If a mobile defect reaches the surface, the defect vanishes. If two defects approach each other, depending on the type of the defects, they can annihilate or, alternatively, form the defect complexes. For example, the interaction of *v* and *i* leads to defects annihilation. The interaction of *v* and *Ar* yields a very stable argon-vacancy complex *vAr* [Fig. 8(d)] with the binding energy $\varepsilon^b_{vAr} = 2.87$ eV[18]. This defect complex is expected to be immobile at room temperature. However, if under annealing *vAr* becomes mobile, a double vacancy-argon complex *2vAr* [Fig. 8(e)] can be formed by the interaction of two complexes *vAr*. Other types of multiple defects can also be formed by the same mechanism: $2vAr + vAr \rightarrow 3vAr$; $3vAr + vAr \rightarrow 4vAr$, and so on. A multiple defect complex *nvAr* [Fig. 8(f)], starting from some $n = N$, can be considered as an Ar-filled nanocavity.

In principle, for an accurate approach, we could also consider the formation of unpaired defect complexes, such as, for example, *vvAr* or *vArAr*. Later on, we will come back to this issue to show that these kinds of defects can be excluded from consideration in our system by a simple physical reason.

Besides the constructive interaction of defects, an inverse process should be taken into account at elevated temperatures. For example, the dissociation of *2vAr* yields two *vAr*, whereas the dissociation of *vAr* yields *v* and *Ar*. A nanocavity *nvAr* can emit *vAr*, leading to a smaller nanocavity (*n*-1)*vAr*.

This brief consideration of different kinds of defects and their transformation from one type to another serves for a clear understanding of how the system is described by our model. Actually, the system is described by a set of differential kinetic equations for the concentration variables C_j corresponding to each defect type *j*. Although this approach can be considered as a standard and can be found elsewhere,[19] the solution of our set of equations is not trivial since the accounting of defect interactions leads to nonlinear equations. Depending on the defect type and various interactions, each equation can also include corresponding specific physical parameters, such as the diffusion coefficient D_j, migration energy $\varepsilon^m{}_j$, dissociation energy $\varepsilon^b{}_j$, and so on.

Generally, the number of equations in this set should correspond to the number of kinetic variables C_j. Because of a variety of different kinds of defects, including different multiple complexes *nvAr*, a solution of the bulky set of many equations can be unacceptably imprecise especially if the physical parameters of defects are not well determined.

Therefore, we used a simplified approach, reducing the number of equations in the set by a proper selection of the

most important ones relevant to the physical processes in our system.

B. Model assumptions

As mentioned above, we use the set of kinetic equations within the framework of a common method, which can be found in other reports. Therefore, we do not show all the equations in detail, presenting only some particular formulas, which are specific to our system. Mainly, we focus our description of the model on physical approximations made within our approach. Using this information and a list of references, the exact expressions describing our system can be easily realized.

Within our approach, we consider that all the multiple defect complexes $nvAr$ with $n \geqslant 3$ can be described in a uniform way as nanocavities with the effective radius R_V. It leaves only the five specific kinds of defects for the separate kinetic variables C_j, namely the vacancies in copper ($j = v$), copper interstitials ($j = i$), Ar interstitials ($j = Ar$), vacancy-argon complexes ($j = vAr$), and double complexes consisting of two vacancies and two argon atoms ($j = 2vAr$). Introducing the nanocavities implies one extra kinetic variable; therefore, we can obtain in total a set of six kinetic equations maximum. Within this set, the description of i, v, and Ar is straightforward since the physical parameters of vacancies and different interstitials are well known. The physical parameters of the defect complexes vAr and $2vAr$ are studied in less detail. Therefore, some of them, for example, the migration energy $\varepsilon^m{}_{vAr}$ of the complex vAr and the dissociation energy $\varepsilon^b{}_{2vAr}$ of the complex $2vAr$, may be found using our experimental data by comparing the calculated kinetic characteristics with the experimental results.

The physical reason to limit the model by selecting only several types of specific defects becomes clear when considering the defect mobility. It is well established that i, v, and Ar are mobile at room temperature. According to the general principals of statistical physics, the complexes $nvAr$ should be much less mobile. After a simple estimate, we can consider that, except for the simplest complexes, as vAr and possibly $2vAr$, all other multiple complexes are immobile. These immobile multiple complexes can be considered as nanocavities, characterized by the macroscopic parameter R_V as well as their size distribution function $f_V(R_V,t)$. The variation of the distribution function can be expressed via variation of the effective radius R_V:

$$\frac{\partial f_V(R_V,t)}{\partial t} = f_0(t)|_{R_V=R_V^0} - \frac{\partial}{\partial R_V}\left(f_V(R_V,t)\frac{dR_V}{dt}\right), \quad (3)$$

where $f_0(t)|_{R_V=R_V^0}$ is the generation rate for the cavities with the minimal radius R_V^0 corresponding to $3vAr$. This generation rate is estimated with the known approach[19–21] as

$$f_0(t)|_{R_V=R_V^0} = \beta_{vAr} D_{vAr} C_{vAr}(t) C_{2vAr}(t)/R_V^0, \quad (4)$$

where $\beta_{vAr} = 4\pi a$ is the parameter of vacancy-argon complex interaction, and a is the mean inter-atomic distance in copper.[22] The distribution function $f_V(R_V,t)$ is included in the set of differential equations since it affects the evolution of C_{vAr} due to adsorbtion-desorbtion processes and vice versa. The volume of the nanocavity and its radius increases due to adsorption of a vacancy-argon complex and decreases due to desorption of vAr complex. The adsorption rate of the vacancy-argon complexes is determined[19] via the diffusion coefficient D_{vAr}, whereas the desorption rate of the vacancy-argon complexes is estimated as a product of the dissociation coefficient χ_V and the number of sites within a cavity, from which a vacancy and argon may leave the cavity. The accounting of these two rates together leads to the following expression for the variation rate of the cavity radius:

$$\frac{dR_V}{dt} = a^2 D_{vAr} C_{vAr}(t) - a\chi_V. \quad (5)$$

This variation rate determines the growth of the nanocavity.

V. CALCULATION RESULTS AND DICUSSION

Although within the framework of our model, the calculation of the nanocavity evolution can be done for a wide temperature range, using the general set of kinetic equations mentioned above, we made one extra step to simplify simulations and make our model robust. We divided the whole temperature range into three temperature intervals. In each temperature interval, the physical processes, which are still not activated, can be excluded from consideration. For example, our experiment shows no formation of nanocavities at room temperature. This means that the complex vAr can be considered as immobile at this temperature. Three reduced sets of equations, each for the corresponding temperature range, are finally obtained. The initial conditions for a chosen temperature interval are well defined at the beginning or, alternatively, taken from the results obtained in the previous temperature interval. This approach significantly reduces the amount of calculations and, at the same time, shows no remarkable deviations in the simulated characteristics.

Consideration of the three temperature intervals is based on the experimental results as described above. The main processes taking place at each temperature interval are schematically shown in Fig. 9. A similar approach is also used in several previous reports.[19–21,23,24] The detailed description of each temperature range is presented below.

A. Temperature range I

Irradiation at $T_{irr} = 300$ K for $t_{irr} = 1800$ s [Figs. 9(a) and 9(b)].

(1) Sputtering of the copper surface reduces the effective dose of argon accepted by the sample.

(2) Under Ar irradiation at this temperature range, only four types of defects can be taken into consideration: the mobile defects v, i, Ar, and the immobile defect complex vAr.

(3) The vacancies and interstitials may diffuse to the surface, which is considered as a sink for all the defects.

(4) By interacting with the interstitial Ar, the vacancies may form vacancy-argon complexes vAr. Alternatively, the vacancies may recombine with the copper interstitials.

The reduced set of equations is solved numerically with well-defined initial conditions. We use the following values of parameters:

(1) The generation rates for the interstitials and vacancies $g_i = g_v = 4.7 \times 10^{22}$ cm^{-3}s^{-1}, as well as for the Ar interstitials $g_{Ar} = 2 \times 10^{20}$ cm^{-3}s^{-1}, have been calculated by the

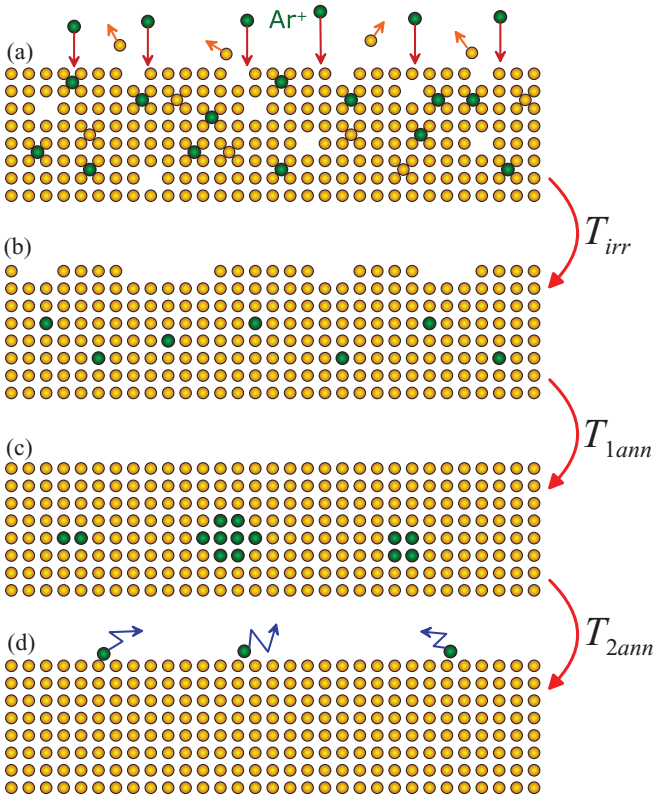

FIG. 9. (Color online) Schematic drawing of the different processes taking place at different temperatures: (a) Irradiation by Ar ions with low fluency produces mainly three types of defects as vacancies and Ar and Cu interstitials. The process of ion etching is also schematically shown; (b) Due to the mobility activated at $T_{irr} =$ 300 K realized in the stage of irradiation, the simplest defects diffuse away or form the immobile vacancy-argon complexes; (c) At the annealing temperature $T_{1ann} = 1000$–1070 K the vAr complexes become mobile and form double vacancy-argon complexes $2vAr$ nucleating further growth of the nanocavities; (d) At the annealing temperature $T_{2ann} = 1075$–1150 K the dissociation of the nanocavities leads to losses of Ar and, finally, to vanishing of the nanocavities.

TRansport of Ions and Recoils in Solid (TRIRS) code,[25] which simulates a single cascade in a binary collision approximation.

(2) The migration energies for interstitials $\varepsilon^m{}_i = 0.12$ eV,[16] vacancies $\varepsilon^m{}_v = 0.7$ eV,[17] and Ar interstitials $\varepsilon^m{}_{Ar} = 0.7$ eV[18] were taken from published reports.

The calculations reveal that the resulting concentrations of the simplest defects such as vacancies v and interstitials of argon Ar and copper i are several orders of magnitude less than the concentration of the vacancy-argon complexes vAr. This result is easy to understand making a simple estimation of diffusion length L_j for the different mobile defects. The diffusion length for v and Ar is of $L_v = L_{Ar} = 50$ nm, which is much higher than the mean defect depth of about 10 nm. It means that the defects, which are not bonded in the vacancy-argon complexes vAr, can easily reach the surface and vanish. Mainly because the complexes vAr remain in the system after irradiation, only they can serve as building elements during nanocavity growth. Because a lack of the simplest defects, there is no opportunity to form the unpaired types of defects, such as, for example, $vvAr$. Therefore, their consideration can be reasonably omitted.

B. Temperature range II

Annealing at $T_{1ann} = 1000$–1070 K for $t_{1ann} = 300$ s [Fig. 9(c)].

(1) At the annealing temperature T_{1ann}, the vacancy-argon complexes vAr become mobile. They can diffuse and interact with each other forming the clusters of two copper vacancies with two argons atoms inside $2vAr$.

(2) The clusters ($2vAr$) of two vacancy-argon complexes may again absorb single vacancy-argon complexes (vAr), one by one, and finally form Ar-filled cavities, which, in this model, are represented by spheres of radius R_V with the size distribution function $f_V(R_V,t)$).

(3) The $2vAr$ clusters can also be dissociated forming two separate vacancy-argon complexes. Clusters of larger sizes, consisting of three or more vacancies and argon atoms, can only absorb the single vacancy-argon complexes at this temperature and, therefore, may only grow. This implies that the dissociation energy ε_V^b of the large clusters of complexes is higher than the dissociation energy of the single or double complexes. Therefore, in the considered temperature range, the dissociation of the clusters of complexes can be excluded.

(4) All the processes take place within the penetration depth of Ar, which is about 10 nm. Within the model frame, the precise profile of depth distribution of defects is not crucial, and the mean value of the depth can be satisfactorily used.

The set of equations adapted for this temperature range has been solved numerically for temperature $T_{1ann} = 1050$ K with initial concentration of vacancy-argon complexes obtained on the previous stage.

By variation in calculation, the value of migration energy $\varepsilon^m{}_{vAr}$ for the vacancy-argon complexes is found to be $\varepsilon^m{}_{vAr} =$ 2.55–2.75 eV.

To our knowledge, there is no available data on the migration energy $\varepsilon^m{}_{vAr}$ of vacancy-argon complexes in metals. The energy values for the two separate parts of this complex in copper are known: for a vacancy[17] $\varepsilon^m{}_v(Cu) = 0.7$ eV and for interstitial argon[18] $\varepsilon^m{}_{Ar}(Cu) = 0.7$ eV. It is remarkable that the migration energy $\varepsilon^m{}_{vAr}(Cu) = 2.55$–$2.75$ eV for the complex found with our simulations is more than 1 eV higher than the sum of these values: $\varepsilon^m{}_{vAr}(Cu) > \varepsilon^m{}_{Ar}(Cu)+\varepsilon^m{}_v(Cu)$. This means that each jump of a vacancy-argon complex (vAr) in a neighboring atomic site is assisted by a larger lattice deformation or more significant local atomic replacement than in the case of separate diffusion of the single vacancy and interstitial Ar.

The similar difference in energies, although not that remarkable, is known for a vacancy and helium atoms in iron.[26] The value of the migration energy of the vacancy-helium complex in iron[26] is $\varepsilon^m{}_{vHe}(Fe) = 1.1$ eV, whereas migration energies for the vacancy and helium[26] are $\varepsilon^m{}_v(Fe) = 0.65$ eV and $\varepsilon^m{}_{He}(Fe) = 0.078$ eV, respectively. Here, the similar relationship between the energies is valid $\varepsilon^m{}_{vHe}(Fe) > \varepsilon^m{}_{He}(Fe)+\varepsilon^m{}_v(Fe)$; however, the energy excess is only about 0.37 eV.

In comparison to similar characteristics for the helium-iron system, the high value of $\varepsilon^m{}_{vAr}(Cu)$ as well its larger difference

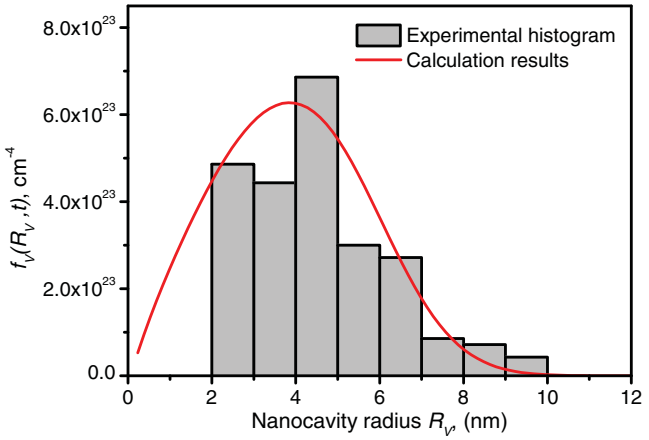

FIG. 10. (Color online) Distribution function $f_V(R_V,t)$ at stage 2 after annealing for 300 s at the temperature $T_{1ann} = 1050$ K. Function $f_V(R_V,t)$ fits the experimental histogram obtained by recalibration of the original data on size distribution (Fig. 7).

from the sum of the vacancy $\varepsilon^m{}_v(Cu)$ and the interstitial atom $\varepsilon^m{}_{Ar}(Cu)$ energies are expected from a qualitative analysis. This can be realized if we take into account the larger size of the argon atom with respect to the helium atom and assume that roughly the properties of the copper and iron crystalline lattice are close to each other.

The dissociation energy ε^b_{2vAr} of the complexes consisting of bivacancy and two argon atoms ($2vAr$) has also been found by its variation in the calculations. The value of this energy is responsible for the maximum position of the size distribution function $f_V(R_V,t)$. By fitting the simulated curve to the recalibrated histogram of size distribution obtained in the experiment (Fig. 10), the value of dissociation energy $\varepsilon^b_{2vAr} =$ 1.10–1.18 eV is found.

The dissociation energy of cavities ε^b_V is considered to be equal to or larger than dissociation energy of vacancy-argon complexes[21], i.e., $\varepsilon^b_V \geqslant \varepsilon^b_{vAr} = 2.85$–$3.04$ eV, implying that the nanocavities are stable in the first annealing stage ($T_{1ann} =$ 1000–1070 K) and they can be dissociated in the second annealing stage ($T_{2ann} =$ 1075–1150 K).

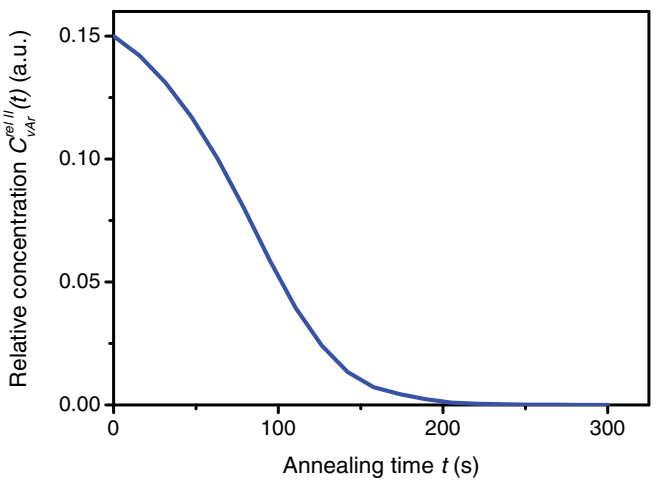

FIG. 11. (Color online) Calculated related concentration of vacancy-argon complexes $C^{relII}_{vAr}(t)$ on annealing time at stage 2.

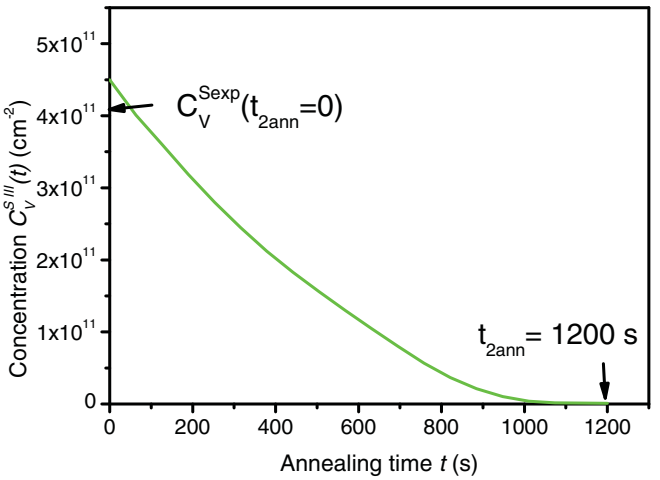

FIG. 12. (Color online) Calculated dependence of 2D concentration of the nanocavities $C^{SIII}_V(t)$ on annealing time at stage 3 at the temperature $T_{2ann} = 1075$ K. The experimental value of concentration at the beginning of annealing as well as the duration of annealing is marked by arrows.

We also calculated the dependency of the concentrations of defects on time. The relative concentration of the vacancy-argon complexes $C^{relII}_{vAr}(t)$ versus time is presented in Fig. 11. It is clearly visible that the concentration $C^{relII}_{vAr}(t)$ decreases approximately to zero after annealing for approximately 200 s. Almost all vAr complexes are spent to form the nanocavities as the model initially assumes.

The calculated size distribution function of nanocavities alongside the experimental histogram is presented in Fig. 10. The three-dimensional concentration of the nanocavities $C_V(t)$ deduced from the distribution function $f_V(R_V,t)$ as $C_V(t) = \int f_V(R_V,t)dR_V$ might be attributed to the 2D concentration of the nanocavities $C^{SII}_V(t)$, which, in fact, was measured in our experiment. This gives $C^{SII}_V \approx 4.5 \times 10^{11}$ cm^{-2} which is slightly larger than the experimental value $C_V^{S\,exp\,II} \approx 4.1 \times 10^{11}$ cm^{-2}. However, one should take into account that the smallest cavities are not observable in the experiment.

The estimated values of migration and dissociation energies, $\varepsilon^m{}_{vAr} = 2.55$–$2.75$ eV and $\varepsilon^b_{2vAr} = 1.10$–$1.18$ eV, are also used in the simulations for the evolution of vacancy-argon complexes at annealing temperatures lower than $T_{1ann} =$ 1000 K. The simulation proves that the nanocavities are not formed at these temperatures, in agreement with the experimental observations discussed above.

C. Temperature range III

Annealing at $T_{2ann} =$ 1075–1150 K for $t_{2ann} = 1200$ s [Fig. 9(d)].

(1) At the elevated annealing temperature $T_{2ann} =$ 1075–1150 K, the dissociation of the nanocavities becomes remarkable, i.e., the single vacancy-argon complexes (vAr) may leave the cavity by overcoming the energy barrier (dissociation energy ε^b_V).

(2) In addition, the vacancy-argon complexes (vAr) also may dissociate forming an argon interstitial and a separate vacancy.

(3) If argon, in both the interstitial states and the complexes, reaches the surface, it evaporates from the sample.

The set of equations for this temperature range gives the time dependence of the 2D concentration $C_V^{SIII}(t)$ of nanocavities presented in Fig. 12. After annealing for approximately 1000 s, which is slightly less than the experimental annealing time $t_{2ann} = 1200$ s, this concentration decreases to zero; the nanocavities disappear, in agreement with the experiment. The decrease of the nanocavity concentration is initiated by two factors: (1) the absence of free vacancy-argon complexes in the copper sample because all these complexes have been spent to build the nanocavities at the annealing at T_{1ann}; and (2) a dissociation of nanocavity starting at the annealing temperature T_{2ann} by increasing the dissociation coefficient χ_V [see Eq. (5)]. Hence, the cavities, releasing the vacancies and argon, are reduced in size. The released argon diffuses in the crystal to the surface and leaves the sample.

VI. CONCLUSIONS

In this work, the formation and evolution of Ar-filled nanocavities in copper has been studied. The description of the full scenario of formation, growth, and decomposition of nanocavities required a specific data set characterizing different kinds of defects induced by Ar-irradiation of the copper crystal. These data have been obtained by carrying out experimental studies, including the XPS and STM and STS analyses of copper sample annealed at different temperature after Ar implantation. The experiment distinguished three characteristic temperature ranges in which various physical processes are activated. Based on the experimental results, a model of nanocavity formation and evolution has been developed. The model considers migration of vacancy-argon complexes as a main mechanism of nucleation and growth of the nanocavities rather than the migration of single vacancies and single interstitial argon. The computer simulations with our model allowed us to estimate the values of the migration energy of the Ar-vacancy complexes, as well as the dissociation energy of the double Ar-vacancy complexes, which are 2.55–2.75 eV and 1.10–1.18 eV, respectively. In spite of making approximations and simplifying assumptions, the model provides a satisfactory agreement with experimental observations in full range of the studied temperature and is qualitatively consistent with data obtained on other metallic system. However, a more realistic approach could be used further with an advanced model based on proper consideration of extra experimental data.

ACKNOWLEDGMENTS

The authors are thankful to P. van Gelder for his valuable remarks improving the presentation. This work is part of the research program of the Dutch Foundation for Fundamental Research on Matter (FOM), which is part of the Netherlands Organization for Scientific Research (NWO). This work is also partially supported by the Russian Fund for Basic Research (RFBR) under Grants No. 11-02-00573-a and 11-02-00727-a.

*Corresponding author: o.kurnosikov@tue.nl

[1] L. Hanley and S. B. Sinnott, Surf. Sci. **500**, 500 (2002).
[2] P. K. Chu, Surf. Coat. Technol. **204**, 2853 (2010).
[3] M. Schmid, W. Hebenstreit, P. Varga, and S. Crampin, Phys. Rev. Lett. **76**, 2298 (1996).
[4] M. Schmid, S. Crampin, and P. Varga J., J. Electr. Spectr. Rel. Phenom. **109**,71 (2000).
[5] O. Kurnosikov, O. A. O. Adam, H. J. M. Swagten, W. J. M. de Jonge, and B. Koopmans, Phys. Rev. B **77**, 125429 (2008).
[6] O. Kurnosikov, J. H. Nietsch, M. Sicot, H. J. M. Swagten, and B. Koopmans, Phys. Rev. Lett. **102**, 066101 (2009).
[7] O. Kurnosikov, H. J. M. Swagten, and B. Koopmans, Phys. Rev. Lett. **106**, 196803 (2011).
[8] C. Sprodowski and K. Morgenstern, Phys. Rev. B **82**, 165444 (2010).
[9] D. G. Armour, Radiat. Eff. Defects Solids **164**, 424 (2009).
[10] J. P. Nozieres, M. Ghidini, N. M. Dempsey, B. Gervais, D. Givord, G. Suran, and J. M. D. Coey, Nucl. Instrum. Methods Phys. Res. B **146**, 250 (1998).
[11] P. Steiner, S. Hüfner, A. J. Freeman, and D.-S. Wang, Solid State Commun. **44**, 619 (1982).
[12] A. Weismann, M. Wenderoth, S. Lounis, P. Zahn, N. Quaas, R. G. Ulbrich, P. H. Dederichs, and S. Blügel, Science **323**, 1190 (2009).
[13] P. H. Citrin and D. R. Hamann, Phys. Rev. B **10**, 4948 (1974).
[14] Y. Baba, H. Yamamoto, and T. A. Sasaki, Surf. Sci. **287**, 806 (1993).
[15] C. Biswas, A. K. Shukla, S. Banik, V. K. Ahire, and S. R. Barman, Nucl. Instrum. Methods Phys. Res. B **212**, 297 (2003).
[16] J. W. Corbett, R. B. Smith, and R. M. Walker, Phys. Rev. **114**, 1460 (1959).
[17] J. Leteurtre, in *Site Characterization and Aggregation of Implanted Atoms in Materials*, edited by A. Perez and R. Coussement (Plenum, New York, 1980).
[18] J. Kuhalainen, M. Manninen, and E. Kautto, J. Phys.: Condens. Matter. **8**, 10317 (1996).
[19] Yu. V. Trushin, *Theory of Radiation Processes in Metal Solid Solutions* (Nova Science Publishers Inc., New York, 1996).
[20] Yu. V. Trushin, D. V. Kulikov, K. L. Safonov, J. W. Gerlach, Th. Höche, and B. Rauschenbach, J. Appl. Phys. **103**, 114904 (2008).
[21] K. L. Safonov, A. A. Schmidt, Yu. V. Trushin, D. V. Kulikov, and J. Pezoldt, Mater. Sci. Forum **433-436**, 591 (2003).
[22] M. Winter, Web Elements: the periodic table on the web, http://www.webelements.com/copper/physics.html. (The University of Sheffield and WebElements Ltd., UK, Copyright 1993–2011).
[23] V. S. Kharlamov, D. V. Kulikov, and Yu. V. Trushin, Vacuum **52**, 407 (1999).
[24] R. Bittner, K. Humer, H. W. Weber, K. Kundzins, A. Sternberg, D. A. Lesnyh, D. V. Kulikov, and Y. V. Trushin, J. Appl. Phys. **96**, 3239 (2004).
[25] Yu. V. Trushin, B. J. Ber, V. S. Kharlarnov, and E. E. Zhurkin, J. Nucl. Mater. **233-237**, 991 (1996).
[26] C. S. Deo, M. A. Okuniewski, S. G. Srivilliputhur, S. A. Maloy, M. I. Baskes, M. R. James, and J. F. Stubbins, J. Nucl. Mater. **361**, 141 (2007).